This manuscript was accepted by Appl. Phys. Lett. Click here to see the version of record.

Magnetic and electrical transport signatures of uncompensated moments in epitaxial thin films of the non-collinear antiferromagnet Mn_3Ir

James M. Taylor * [1], Edouard Lesne [1], Anastasios Markou [2], Fasil Kidane Dejene [1], Pranava Keerthi Sivakumar [1], Simon Pöllath [3], Kumari Gaurav Rana [1], Neeraj Kumar [1], Chen Luo [4,5], Hanjo Ryll [4], Florin Radu [4], Florian Kronast [4], Peter Werner [1], Christian H. Back [3,5], Claudia Felser [2], Stuart S. P. Parkin † [1]

[1] Max Planck Institute of Microstructure Physics, Weinberg 2, 06120 Halle (Saale), Germany
[2] Max Planck Institute for Chemical Physics of Solids, Nöthnitzer Str. 40, 01187 Dresden, Germany
[3] Institute of Experimental Physics, University of Regensburg, 93040 Regensburg, Germany
[4] Helmholtz-Zentrum Berlin for Materials and Energy, Albert Einstein Str. 15, Berlin 12489, Germany
[5] Institute of Experimental Physics of Functional Spin Systems, Technical University Munich, James-Franck-Str. 1, 85748 Garching b. München, Germany

Abstract

Non-collinear antiferromagnets, with either an $L1_2$ cubic crystal lattice (e.g. Mn_3Ir and Mn_3Pt) or a $D0_{19}$ hexagonal structure (e.g. Mn_3Sn and Mn_3Ge), exhibit a number of phenomena of interest to topological spintronics. Amongst the cubic systems, for example, tetragonally distorted Mn_3Pt exhibits an intrinsic anomalous Hall effect (AHE). However, Mn_3Pt only enters a non-collinear magnetic phase close to the stoichiometric composition and at suitably large thicknesses. Therefore, we turn our attention to Mn_3Ir, the material of choice for use in exchange bias heterostructures. In this letter, we investigate the magnetic and electrical transport properties of epitaxially grown, face-centered-cubic γ-Mn_3Ir thin films with (111) crystal orientation. Relaxed films of 10 nm thickness exhibit an ordinary Hall effect, with a hole-type carrier concentration of $(1.500 \pm 0.002) \times 10^{23}$ cm^{-3}. On the other hand, TEM characterization demonstrates that ultrathin 3 nm films grow with significant in-plane tensile strain. This may explain a small net magnetic moment, observed at low temperatures, shown by XMCD spectroscopy to arise from uncompensated Mn spins. Of the order 0.02 μ_B / atom, this dominates electrical transport behavior, leading to a small AHE and negative magnetoresistance. These results are discussed in terms of crystal microstructure and chiral domain behavior, with spatially resolved XML(C)D-PEEM supporting the conclusion that small antiferromagnetic domains, < 20 nm in size, of differing chirality account for the absence of observed Berry curvature driven magnetotransport effects.

* james.taylor@mpi-halle.mpg.de
† stuart.parkin@mpi-halle.mpg.de

This manuscript was accepted by Appl. Phys. Lett. Click here to see the version of record.

Antiferromagnetic (AF) spintronics is a growing research field [1], motivated by a number of potential advantages for applications including ultrafast magnetization dynamics [2] and improved stability against external perturbations at reduced dimensions. For example, synthetic antiferromagnetic structures (SAFs) [3] are already employed to eliminate magnetostatic fields in spin-valve sensors [4] and magnetic tunnel junction (MTJ) memory bits [5]. Furthermore, an efficient current-driven domain-wall motion has been demonstrated in such SAFs [6] by utilizing the chirality of the magnetic structure [7].

Indeed, chiral spin textures play a key role in the emerging field of topological AF spintronics [8]. Of particular interest are the non-collinear AFs Mn_3X (X = Ir, Pt, Sn, Ge), which can stabilize with either a face-centered-cubic (fcc) or a hexagonal crystal structure. The symmetry breaking non-collinear spin texture of these materials, combined with spin-orbit coupling, gives rise to a Berry curvature driven effective field, that is predicted to generate an intrinsic anomalous Hall effect (AHE) [9, 10]. In the case of cubic Mn_3Ir, a facet-dependent spin Hall effect (SHE) emerging from the same origin has been discovered [11]. Whilst this intrinsic SHE is even with respect to the handedness of topological AF order, contributions to the AHE will cancel out over domains with opposite chirality of spin texture [12].

Experimental measurements of the intrinsic AHE have been realized in bulk single crystals of hexagonal non-collinear AFs, namely Mn_3Sn [13] and Mn_3Ge [14]. This has been enabled by the small in-plane magnetic moment exhibited by these materials, also demonstrated in epitaxial thin films of Mn_3Sn [15], which arises from geometric frustration of the inverse triangular spin texture. Alignment of this weak magnetization via an external magnetic field in turn coherently orientates the AF order throughout the material, driving it into a dominant chiral domain state [16].

Such control of AF domains is challenging in the fcc non-collinear systems, which are normally fully compensated with strong internal anisotropy fields [17]. However, Liu *et al.* [18] have recently discovered a large AHE in Mn_3Pt films epitaxially grown with in-plane tensile strain on $BaTiO_3$ substrates. Mn_3Pt undergoes a first-order magnetic phase transition from the non-collinear to a collinear AF state above ≈ 360 K. AHE is only observed below this transition temperature, where a small uncompensated magnetization is also measured. The size of this net moment correlates with the magnitude of Berry curvature driven AHE and shows a dependence on the degree of tetragonal distortion of the films, although the exact relationship between them (including the role of chiral domain manipulation) remains open to further study.

This manuscript was accepted by Appl. Phys. Lett. Click here to see the version of record.

Whilst the magnetic phase transition of Mn_3Pt has allowed the important demonstration of electric field control of this topological AHE, by applying additional piezoelectric strain to move between the collinear and non-collinear states [18], it also presents an upper limit to the operating temperature in resulting spintronic structures. On the other hand, the closely related cubic non-collinear AF Mn_3Ir can be stabilized with a triangular spin texture below its high Néel temperature, $T_N \approx 700$ K [19], over a broad composition range in the phase diagram [20].

Whilst Mn_3Ir has previously been utilized as an exchange bias pinning layer in heterostructures with ferromagnets (FM) [21, 22], and subsequently spin-orbit torques studied in such bilayers [23, 24], further understanding of the magnetotransport properties of Mn_3Ir alone are required before its potential implementation into future chiral spintronic applications [25-27]. Therefore, in this letter we explore further the subtle interplay between crystal microstructure, uncompensated moments and electrical transport properties in this non-collinear AF. In order to elucidate the behavior of Berry curvature driven phenomena in these materials, thin film samples with high-quality crystal structure are required, whilst the commercial realization of AF spintronic devices requires deposition using fast and flexible techniques [28].

To this end, the epitaxial films utilized here were grown by magnetron sputtering according to our recipe published in Ref. [29]. Mn_3Ir films with (111) planes parallel to the substrate surface were selected for further study, grown with sample structure: Al_2O_3 (0001) [Substrate] / TaN (111) [5 nm] / $Mn_{(0.72 \pm 0.03)}Ir_{(0.28 \pm 0.03)}$ (111) [3 or 10 nm] / TaN [2.5 nm]. The two different sample thicknesses were chosen to display different structural properties, whilst both having a T_N above room temperature (RT) [24]. Comprehensive characterization is detailed in Ref. [29], demonstrating that these films grow in an fcc γ-Mn_3Ir phase and suggesting a non-collinear magnetic structure [19].

As detailed in the Supplementary Material, 10 nm Mn_3Ir (111) films grow fully relaxed, with a large grain size in the lateral direction of ≥ 20 nm. In the case of 3 nm ultrathin films, high-resolution TEM operated at 300 kV (FEI Titan 80-300) was used to further analyze crystal structure. Fig. 1(a) shows a typical micrograph of the epitaxial growth of <111> oriented Mn_3Ir, with sharp interfaces and uniform thickness. Examples of grain boundary defects are highlighted, indicating slightly smaller laterally oriented grains in these ultrathin films. Indeed, examination of different regions of the TEM lamella allows an estimation of lateral grain size of 15 to 20 nm.

This manuscript was accepted by Appl. Phys. Lett. Click here to see the version of record.

The inset of Fig. 1(a) displays a fast Fourier transform diffractogram for the 3 nm Mn_3Ir (111) film, taken from the marked area. Indexing of Mn_3Ir (111) and (002) diffraction peaks allows the calculation of out-of-plane, OP (d_{111}), and in-plane, IP ($d_{\bar{1}\bar{1}2} = \sqrt{2/3}\, d_{002}$), lattice spacing respectively. In the OP direction, the lattice plane separation, d_{111} = (2.19 ± 0.09) Å, agrees within uncertainty with the bulk value (2.182 Å). Meanwhile, the estimated IP crystal lattice spacing is $d_{\bar{1}\bar{1}2}$ = (1.9 ± 0.1) Å. In spite of the high uncertainty in this measurement, which arises from the low intensity of the diffractogram extracted from such an ultrathin layer, it is significantly larger than the bulk value (1.543 Å). This indicates that the 3 nm Mn_3Ir (111) film grows with appreciable IP strain. A volume expansion of the unit cell results, also previously found in < 5 nm thick films of Mn-based Heusler compounds [30, 31]. This is expected to lead to a modification of magnetic properties (as observed, for example, in the non-collinear AF Mn_3Ge under hydrostatic pressure [32]) due to changing interatomic distances between Mn atoms [33].

Characterization of these samples' magnetism using SQUID vibrating sample magnetometry proved challenging, as previously reported for ultrathin ferrimagnetic films [30] and discussed further in the Supplementary Material. Instead, direct measurements of the films' magnetic moment (m) were performed using X-ray magnetic circular dichroism (XMCD) spectroscopy at the VEKMAG endstation of the PM2 beamline at BESSY [34]. X-ray absorption spectra (XAS) were recorded around the Mn-L_3 edge in total electron yield mode (shown in the inset of Fig. 1(b)), using alternating right- and left-circularly polarized X-rays (σ^+ and σ^- respectively), at a temperature T = 10 K. Fig. 1(b) displays the resulting XMCD signal, $(\sigma^+ - \sigma^-)/(\sigma^+ + \sigma^-)$, as a function of OP applied magnetic field along the [111] direction, $\mu_0 H$. In the case of a 10 nm Mn_3Ir (111) film, a small linear response of Mn magnetic moment (calculated using the XMCD sum rules [35]) is observed, explained by their slight canting out of the (111) plane under the influence of an external magnetic field. Due to the high magnetic anisotropy of Mn_3Ir [17], we estimate that the fields used during these experiments remain well below any spin-flip transition.

For a 3 nm Mn_3Ir (111) film, an XMCD signal which is hysteretic for $\mu_0 H < 2$ T is measured, with a coercivity of approximately 0.3 T. A subtle plateau in XMCD signal (where low-field hysteretic behavior reverts to a linear response) is seen at around 0.5%, corresponding to a net Mn moment of 0.02 μ_B / atom. This demonstrates a small saturating component of magnetization in ultrathin Mn_3Ir (111) films, which can be manipulated by an external magnetic field and arises from uncompensated Mn spins. Since both chemical composition and defect density are similar in 10

This manuscript was accepted by Appl. Phys. Lett. Click here to see the version of record.

nm and 3 nm thick samples, this effect could be interface driven, for example, by a re-orientation of non-collinear AF structure [36]. However, no similar effect has been observed in ultrathin poly-crystalline $Mn_{0.8}Ir_{0.2}$ films [23]. Therefore, the origin of this uncompensated moment may instead be strain in our epitaxial 3 nm Mn_3Ir (111) films. This is consistent with the results of Liu *et al*. [18], and can be explained by the slightly increased interatomic distance beginning to favor parallel coupling of Mn spins [37]. Modification of remnant magnetization by IP strain has also been reported in epitaxially distorted thin films of the non-collinear AF Mn_3Ga [31].

The thin films were then patterned into Hall bars, using electron beam lithography and Ar ion etching, with dimensions ranging from 150 × 50 μm^2 down to 3 × 1 μm^2. Current (I_c = 200 μA) flow was directed along Hall bars fabricated in different IP crystalline directions. The inset of Fig. 2(b) displays the electrical measurement geometry, for an exemplar 15 × 5 μm^2 device. Previous magnetotransport measurements in polycrystalline $Mn_{0.8}Ir_{0.2}$ utilized anisotropic magnetoresistance (AMR) [25] or tunneling-AMR [26] to detect AF order. In our case, longitudinal (ρ_{xx}) and transverse (ρ_{xy}) resistivity were measured at different temperatures, as a function of external magnetic field applied OP.

Fig. 2(a) records measurements of transverse resistivity in a 150 × 50 μm^2 Hall bar of a 3 nm Mn_3Ir (111) film. We observe an anomalous-type behavior of ρ_{xy} at 2 K, saturating at comparable fields to the hysteretic part of the XMCD signal. The inset of Fig. 2(a) shows this is accompanied by a negative longitudinal MR, $([\rho_{xx}(\mu_0 H)-\rho_{xx}(0)]/\rho_{xx}(0))\times 100\%$, which points to a magnetic origin, namely the presence of uncompensated Mn moments, for the exhibited AHE in strained ultrathin Mn_3Ir (111) films. We find comparable AHE across devices of different sizes, down to the smallest 3 × 1 μm^2 Hall bars, as shown in Supplementary Fig. S2(a). Similar electrical measurements of uncompensated Mn spins have been made at RT by Kosub *et al*. [27].

In our case, as temperature is increased above 50 K, both AHE and negative MR are replaced by an ordinary Hall effect and positive MR respectively, demonstrated for a measurement at 300 K in Fig. 2(a). We attribute this change in behavior to a vanishing of the strain-induced uncompensated moment at higher temperatures. In spite of this, Supplementary Fig S2(a) shows that low temperature transport properties are not modified after cooling from 400 K in a 9 T magnetic field along the [111] axis. This implies that samples remain antiferromagnetic up to and above RT (i.e. have respective T_N > 400 K), because it is known that field cooling analogous polycrystalline $Mn_{0.8}Ir_{0.2}$ films through T_N can modify their electrically-detected AF order [38].

This manuscript was accepted by Appl. Phys. Lett. Click here to see the version of record.

These different temperature dependencies imply that strain-mediated uncompensated Mn moments are decoupled from the bulk triangular AF order. They are therefore unable to coherently orient spin texture under external magnetic field and thus induce Berry curvature driven AHE, which would be expected to produce a larger ρ_{xy} signal, as is the case for Mn_3Pt [18]. In addition, the magnitude of ρ_{xy} measured in 3 nm Mn_3Ir (111) films is smaller than that for 10 nm thick samples, reported below. We can attribute this to a short mean free path of electrons (as calculated in the Supplementary Material), meaning interface scattering will contribute significantly to resistivity in the 3 nm films, in turn acting to reduce transverse voltage. Furthermore, a sign change of ρ_{xy} (with respect to 10 nm films), indicates the presence of electron-like carriers in the 3 nm ultrathin regime. Such a change in charge carrier type indicates a modification of band structure between the two different film thicknesses. This can be explained by considering the variation of longitudinal resistivity with temperature, displayed in the inset of Supplementary Fig. S2(a). Whilst scattering is defect dominated in 10 nm Mn_3Ir (111), the actual band structure at the Fermi level may be sensitive to, for example, the observed structural changes in 3 nm Mn_3Ir (111).

Fig. 2(b) shows the transverse resistivity of a 10 nm Mn_3Ir (111) film measured at 300 K and 2 K in a 15 × 5 μm^2 Hall bar fabricated along the $[\bar{1}\bar{1}2]$ crystallographic axis. A positive linear response of ρ_{xy} is measured across the temperature range, indicating hole-type charge carriers. Fitting the gradient ($\rho_{xy}/\mu_0 H$) of this ordinary Hall effect at RT allows determination of the carrier concentration, h = (1.500 ± 0.002) × 10^{23} cm^{-3}. As well as demonstrating a lack of uncompensated Mn moments, such an ordinary Hall effect is consistent with an absence of Berry curvature driven AHE. This is because the moderate magnetic fields applied in this experiment are insufficient to drive Mn_3Ir into a single chiral domain state. Instead, AHE cancels over multiple degenerate AF domains with opposing orientation of triangular spin texture [11].

To investigate this further, ρ_{xy} was measured in Hall bar devices fabricated along different crystalline directions, because the intrinsic AHE is predicted to by highly anisotropic [12]. However, a linear Hall effect is observed along all crystallographic axes, demonstrated in Supplementary Fig. S2(b) for the example of a 15 × 5 μm^2 Hall bar fabricated along the $[1\bar{2}1]$ crystalline direction. This isotropic behavior suggests any intrinsic AHE may cancel over multiple differently oriented AF domains, which follow the six-fold symmetry of the epitaxial crystal structure. To isolate individual chiral domains, we therefore performed measurements of ρ_{xy} in devices of differing

This manuscript was accepted by Appl. Phys. Lett. Click here to see the version of record.

size. Again, the ordinary Hall effect found in all devices points to AF domain size in epitaxial 10 nm Mn_3Ir (111) thin films being significantly smaller than the lowest Hall bar dimension tested (1 μm).

Therefore, in an attempt to elucidate the chiral domain structure of 10 nm Mn_3Ir (111) thin films, we performed X-ray magnetic linear (circular) dichroism photo-emission electron microscopy, XML(C)D-PEEM (or X-PEEM), at beamline UE49_PGM at BESSY. Experimental details are described in the Supplementary Material. Fig. 3(a) shows an XMCD-PEEM image, taken at the Mn-L_3 edge, at 45 K with no applied external magnetic field. For this film without remnant Mn moment, no net XMCD signal is observed. Instead, only small intensity fluctuations at the resolution limit of the electron microscope create contrast in the image.

XMLD-PEEM imaging has been shown to exhibit contrast between domains with orthogonal Néel vector orientations in collinear AFs [39, 40]. We postulate that, in the same way, differences in orientation between the linearly polarized X-rays and the Néel vector defining the chirality of the triangular spin texture would lead to a difference in absorption between opposite chirality AF domains. Fig. 3(b) shows such an XMLD-PEEM image measured at the Mn-L_3 edge for the same 10 nm Mn_3Ir (111) sample; no XMLD contrast is discerned above the sample surface topography background. Possible reasons are discussed in the Supplementary Material, one of which may be that AF domains are smaller than the resolution limit of the PEEM (≈ 20 nm), which will indeed be the case if they are correlated with the grain size in the film measured using TEM.

Finally, in an attempt to enlarge chiral domains in Mn_3Ir to an observable size, exchange bias was utilized to introduce a preferential AF domain orientation through coupling to a ferromagnetic (FM) layer [22]. X-PEEM was therefore imaged at both the Ni-L_3 and Mn-L_3 edges in a 3nm Mn_3Ir (111) / 5 nm $Ni_{80}Fe_{20}$ bilayer. We have demonstrated that such heterostructures show large exchange anisotropy after cooling below their blocking temperature of 40 K [29]. Fig. 3(c) exhibits an approximately equal distribution of oppositely oriented FM domains in an XMCD-PEEM image recorded at the Ni-L_3 edge at RT. After cooling the bilayer to 70 K under a 20 mT IP magnetic field, Fig. 3(d) displays a repeat XMCD-PEEM image of the same area, in which the FM domains have grown but no preferential domain direction has been set. This is likely due to the bilayer not having passed through its blocking temperature. Finally, XMCD- and XMLD-PEEM images were recorded at the Mn-L_3 edge after this IP field cooling routine, shown in Figs. 3(e) and (f) respectively. No uncompensated Mn spins are observed at the interface, as expected if the

This manuscript was accepted by Appl. Phys. Lett. Click here to see the version of record.

temperature is not low enough to induce large exchange bias [21]. Finally, no AF domains of differing chirality are resolved, which may be due to the concomitant difficulty of observing the buried interface through a 5 nm $Ni_{80}Fe_{20}$ layer [41] combined with the intrinsic spatial resolution limit of X-PEEM discussed above.

In conclusion, we studied the magnetic and electrical properties of fully relaxed 10 nm Mn_3Ir (111) samples, and of ultrathin films exhibiting significant IP lattice distortion. This tensile strain may be the origin of an uncompensated Mn magnetic moment observed by XMCD spectroscopy. Because of this net Mn magnetization, the 3 nm Mn_3Ir (111) films demonstrate a small negative MR and AHE at low temperature. On the other hand, 10 nm Mn_3Ir (111) films exhibit ordinary Hall effect, which is isotropic with respect to IP crystallographic direction. A lack of Berry curvature driven electrical transport effects can be explained by the presence of multiple AF domains of differing triangular spin texture chirality, suggested by XML(C)D-PEEM imaging to be correlated with film grain size and thus < 20 nm. Our results illuminate the intimate connection between crystal structure, uncompensated spins and magnetotransport properties, therefore informing the further implementation of non-collinear Mn_3X thin films in *chiralitronic* devices.

Supplementary Material

See supplementary material for characterization of 10 nm Mn_3Ir (111) thin films, supporting magnetic and electrical transport measurements, and details of X-PEEM experimental procedures.

Acknowledgments

We acknowledge Helmholtz-Zentrum Berlin (HZB) for synchrotron beamtime at UE49_PGM SPEEM (proposal 181-06569) and at PM2 VEKMAG (proposal 171-04784). Financial support for the VEKMAG project and for the PM2 VEKMAG beamline are provided by the German Federal Ministry for Education and Research (BMBF 05K10PC2, 05K10WR1, 05K10KE1) and by HZB, with Steffen Rudorff thanked for technical support. This work was partially funded by ASPIN (EU H2020 FET open grant 766566).

Figure Captions

FIG. 1. (a) TEM image of a 3 nm Mn_3Ir (111) film, viewed along the $[1\bar{1}0]$ zone axis, with in-plane crystallographic directions indicated and grain boundaries highlighted by dashed lines (inset shows diffractogram from region marked by green box). (b) XMCD measured for 10 nm and 3 nm Mn_3Ir (111) films at 10 K (inset shows XAS spectra recorded at the Mn-L_3 edge using right- and left-circularly polarized X-rays after sweeping magnetic field to -8 T, and the resulting XMCD spectrum, for a 3 nm thin film).

FIG. 2. (a) Hall effect for a 3 nm Mn_3Ir (111) film in a 150 × 50 μm^2 Hall bar directed along $[\bar{1}\bar{1}2]$ at 300 K and at 2 K (inset shows variation in longitudinal magnetoresistance over the same magnetic field range). (b) Hall effect for a 10 nm Mn_3Ir (111) film in a 15 × 5 μm^2 Hall bar directed along $[\bar{1}\bar{1}2]$ at 300 K and at 2 K (inset shows an optical image of example patterned device with measurement geometry indicated).

FIG. 3. XPEEM images (5 × 5 μm^2) measured in a 10 nm Mn_3Ir (111) film using (a) XMCD and (b) XMLD at the Mn-L_3 edge; and in a 3 nm Mn_3Ir (111) / 5 nm $Ni_{80}Fe_{20}$ bilayer using XMCD at the Ni-L_3 edge both at (c) 300 K and (d) 70 K after 20 mT IP field cooling, and using (e) XMCD and (f) XMLD at the Mn-L_3 edge after 20 mT IP field cooling.

References

1. V. Baltz, A. Manchon, M. Tsoi, T. Moriyama, T. Ono and Y. Tserkovnyak, Rev. Mod. Phys. **90** (1), 015005 (2018).
2. A. J. Sievers and M. Tinkham, Phys. Rev. **129** (4), 1566-1571 (1963).
3. S. S. P. Parkin, N. More and K. P. Roche, Phys. Rev. Lett. **64** (19), 2304-2307 (1990).
4. S. S. P. Parkin, J. Xin, C. Kaiser, A. Panchula, K. Roche and M. Samant, Proc. IEEE **91** (5), 661-680 (2003).
5. S. S. P. Parkin, K. P. Roche, M. G. Samant, P. M. Rice, R. B. Beyers, R. E. Scheuerlein, E. J. O'Sullivan, S. L. Brown, J. Bucchigano, D. W. Abraham, Y. Lu, M. Rooks, P. L. Trouilloud, R. A. Wanner and W. J. Gallagher, J. Appl. Phys. **85** (8), 5828-5833 (1999).
6. S. H. Yang, K. S. Ryu and S. S. P. Parkin, Nat. Nanotechnol. **10** (3), 221-226 (2015).
7. K. S. Ryu, L. Thomas, S. H. Yang and S. S. P. Parkin, Nat. Nanotechnol. **8** (7), 527-533 (2013).
8. L. Šmejkal, Y. Mokrousov, B. Yan and A. H. MacDonald, Nat. Phys. **14** (3), 242-251 (2018).
9. H. Chen, Q. Niu and A. H. MacDonald, Phys. Rev. Lett. **112** (1), 017205 (2014).
10. J. Kübler and C. Felser, Europhys. Lett. **108** (6), 67001 (2014).
11. W. Zhang, W. Han, S. H. Yang, Y. Sun, Y. Zhang, B. Yan and S. S. P. Parkin, Sci. Adv. **2** (9), e1600759 (2016).
12. Y. Zhang, Y. Sun, H. Yang, J. Železný, S. S. P. Parkin, C. Felser and B. Yan, Phys. Rev. B **95** (7), 075128 (2017).
13. S. Nakatsuji, N. Kiyohara and T. Higo, Nature **527** (7577), 212-215 (2015).
14. A. K. Nayak, J. E. Fischer, Y. Sun, B. Yan, J. Karel, A. C. Komarek, C. Shekhar, N. Kumar, W. Schnelle, J. Kübler, C. Felser and S. S. P. Parkin, Sci. Adv. **2** (4), e1501870 (2016).
15. A. Markou, J. M. Taylor, A. Kalache, P. Werner, S. S. P. Parkin and C. Felser, Phys. Rev. Mater. **2** (5), 051001(R) (2018).
16. T. Higo, H. Man, D. B. Gopman, L. Wu, T. Koretsune, O. M. J. van 't Erve, Y. P. Kabanov, D. Rees, Y. Li, M. T. Suzuki, S. Patankar, M. Ikhlas, C. L. Chien, R. Arita, R. D. Shull, J. Orenstein and S. Nakatsuji, Nat. Photonics **12** (2), 73-78 (2018).
17. L. Szunyogh, B. Lazarovits, L. Udvardi, J. Jackson and U. Nowak, Phys. Rev. B **79** (2), 020403 (2009).
18. Z. Q. Liu, H. Chen, J. M. Wang, J. H. Liu, K. Wang, Z. X. Feng, H. Yan, X. R. Wang, C. B. Jiang, J. M. D. Coey and A. H. MacDonald, Nat. Electron. **1** (3), 172-177 (2018).
19. A. Kohn, A. Kovács, R. Fan, G. J. McIntyre, R. C. C. Ward and J. P. Goff, Sci. Rep. **3**, 2412 (2013).
20. K. Sasao, R. Y. Umetsu, K. Fukamichi and A. Sakuma, J. Alloys and Compd. **352** (1), 21-25 (2003).
21. H. Ohldag, A. Scholl, F. Nolting, E. Arenholz, S. Maat, A. T. Young, M. Carey and J. Stöhr, Phys. Rev. Lett. **91** (1), 017203 (2003).
22. T. Eimüller, T. Kato, T. Mizuno, S. Tsunashima, C. Quitmann, T. Ramsvik, S. Iwata and G. Schütz, Appl. Phys. Lett. **85** (12), 2310-2312 (2004).
23. H. Reichlová, D. Kriegner, V. Holý, K. Olejník, V. Novák, M. Yamada, K. Miura, S. Ogawa, H. Takahashi, T. Jungwirth and J. Wunderlich, Phys. Rev. B **92** (16), 165424 (2015).
24. L. Frangou, S. Oyarzún, S. Auffret, L. Vila, S. Gambarelli and V. Baltz, Phys. Rev. Lett. **116** (7), 077203 (2016).
25. R. Galceran, I. Fina, J. Cisneros-Fernández, B. Bozzo, C. Frontera, L. López-Mir, H. Deniz, K. W. Park, B. G. Park, L. Balcells, X. Martí, T. Jungwirth and B. Martínez, Sci. Rep. **6**, 35471 (2016).
26. B. G. Park, J. Wunderlich, X. Martí, V. Holý, Y. Kurosaki, M. Yamada, H. Yamamoto, A. Nishide, J. Hayakawa, H. Takahashi, A. B. Shick and T. Jungwirth, Nat. Mater. **10** (5), 347-351 (2011).
27. T. Kosub, M. Kopte, F. Radu, O. G. Schmidt and D. Makarov, Phys. Rev. Lett. **115** (9), 097201 (2015).
28. A. A. Jara, I. Barsukov, B. Youngblood, Y. Chen, J. Read, H. Chen, P. Braganca and I. N. Krivorotov, IEEE Magn. Lett. **7**, 1-5 (2016).
29. J. M. Taylor, E. Lesne, A. Markou, F. K. Dejene, B. Ernst, A. Kalache, K. G. Rana, N. Kumar, P. Werner, C. Felser and S. S. P. Parkin, arXiv:1903.05539 (2019).
30. A. Köhler, I. Knez, D. Ebke, C. Felser and S. S. P. Parkin, Appl. Phys. Lett. **103** (16) (2013).
31. J. T. Holguín-Momaca, C. J. Muñoz-Carnero, H. Sharma, C. R. Santillán-Rodríguez, J. A. Matutes-Aquino, C. V. Tomy and S. F. Olive-Méndez, J. Mag. Mag. Mater. **471**, 329-333 (2019).
32. A. S. Sukhanov, S. Singh, L. Caron, T. Hansen, A. Hoser, V. Kumar, H. Borrmann, A. Fitch, P. Devi, K. Manna, C. Felser and D. S. Inosov, Phys. Rev. B **97** (21), 214402 (2018).
33. R. M. Gutiérrez-Pérez, J. T. Holguín-Momaca, J. T. Elizalde-Galindo, F. Espinosa-Magaña and S. F. Olive-Méndez, J. Appl. Phys. **117** (12) (2015).
34. T. Noll and F. Radu, in *Proc. of MEDSI2016, Barcelona, Spain, September 2016*, edited by V. R. W. Schaa (JACoW, Geneva, Switzerland, 2017), pp. 370-373.
35. C. T. Chen, Y. U. Idzerda, H. Lin, N. V. Smith, G. Meigs, E. Chaban, G. H. Ho, E. Pellegrin and F. Sette, Phys. Rev. Lett. **75** (1), 152-155 (1995).
36. F. Hellman, A. Hoffmann, Y. Tserkovnyak, G. S. D. Beach, E. E. Fullerton, C. Leighton, A. H. MacDonald, D. C. Ralph, D. A. Arena, H. A. Dürr, P. Fischer, J. Grollier, J. P. Heremans, T. Jungwirth, A. V. Kimel, B. Koopmans, I. N. Krivorotov, S. J. May, A. K. Petford-Long, J. M. Rondinelli, N. Samarth, I. K. Schuller, A. N. Slavin, M. D. Stiles, O. Tchernyshyov, A. Thiaville and B. L. Zink, Rev. Mod. Phys. **89** (2), 025006 (2017).
37. N. Yamada, J. Phys. Soc. Jpn. **59**, 273 (1990).
38. D. Petti, E. Albisetti, H. Reichlová, J. Gazquez, M. Varela, M. Molina-Ruiz, A. F. Lopeandía, K. Olejník, V. Novák, I. Fina, B. Dkhil, J. Hayakawa, X. Martí, J. Wunderlich, T. Jungwirth and R. Bertacco, Appl. Phys. Lett. **102** (19), 192404 (2013).
39. P. Wadley, S. Reimers, M. J. Grzybowski, C. Andrews, M. Wang, J. S. Chauhan, B. L. Gallagher, R. P. Campion, K. W. Edmonds, S. S. Dhesi, F. Maccherozzi, V. Novak, J. Wunderlich and T. Jungwirth, Nat. Nanotechnol. **13** (5), 362-365 (2018).
40. A. A. Sapozhnik, M. Filianina, S. Y. Bodnar, A. Lamirand, M. A. Mawass, Y. Skourski, H. J. Elmers, H. Zabel, M. Kläui and M. Jourdan, Phys. Rev. B **97** (13), 134429 (2018).
41. Y. Wang, C. Song, G. Wang, J. Miao, F. Zeng and F. Pan, Adv. Funct. Mater. **24** (43), 6806-6810 (2014).

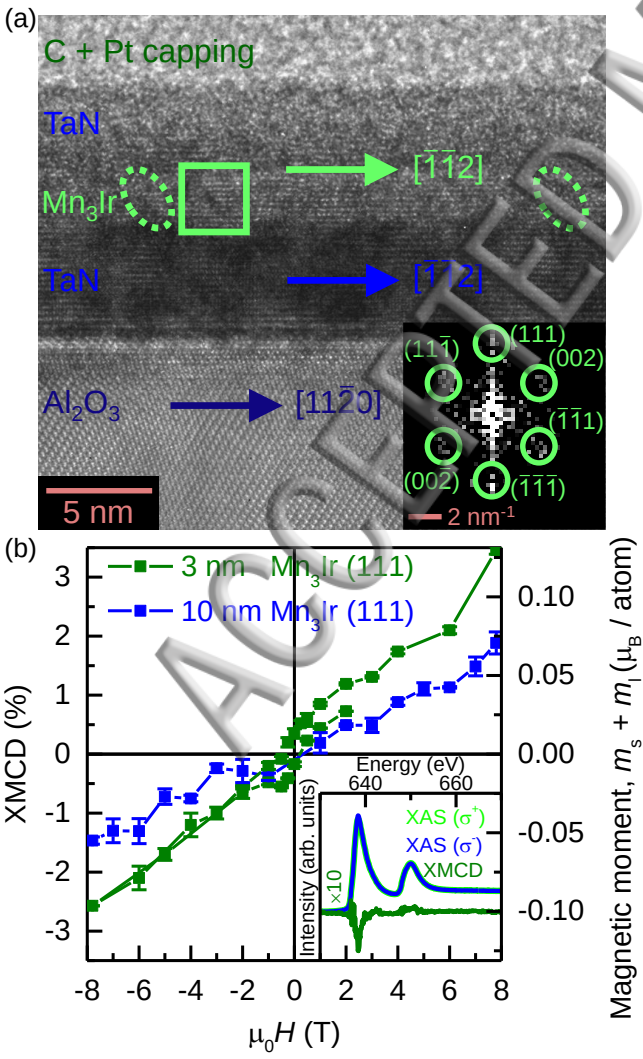
(a)
C + Pt capping
TaN
Mn3Ir
[1̄1̄2]
TaN
[1̄12]
Al2O3
[11̄20]
(111)
(11̄1)
(002)
(1̄11̄)
(002̄)
(1̄11)
2 nm-1
5 nm
(b)
3 nm Mn3Ir (111)
10 nm Mn3Ir (111)
XMCD (%)
Magnetic moment, ms + ml (μB / atom)
μ0H (T)
Energy (eV)
640
660
Intensity (arb. units)
XAS (σ+)
XAS (σ−)
XMCD
×10

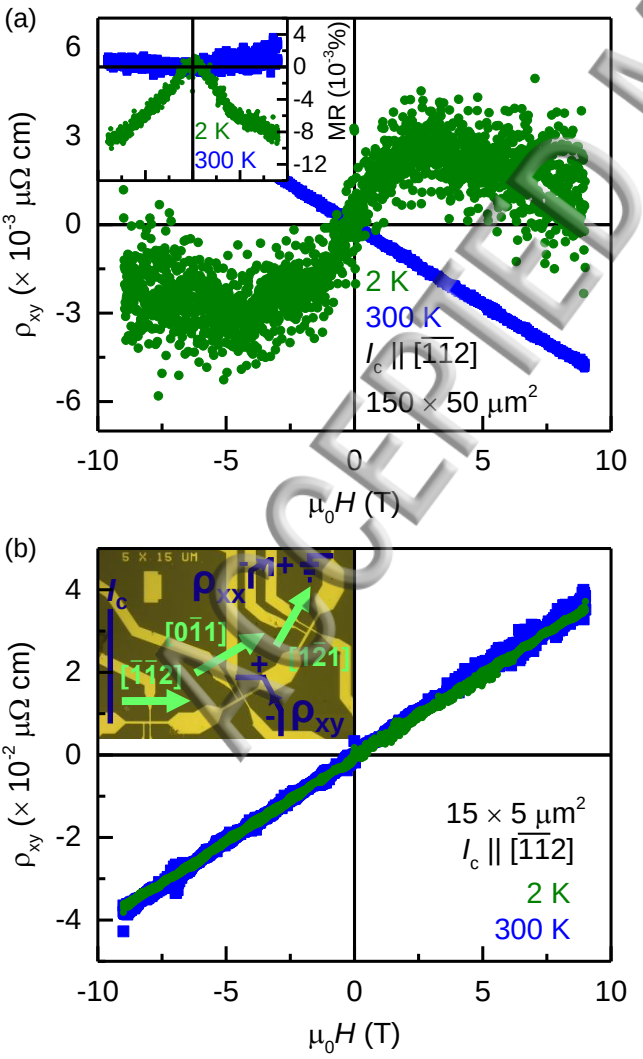
(a)
6
3
0
-3
-6
ρ_{xy} ($\times$ 10^{-3} $\mu\Omega$ cm)
4
0
-4
-8
-12
MR (10^{-3}%)
2 K
300 K
2 K
300 K
I_c || [$\bar{1}\bar{1}2$]
150 $\times$ 50 μm^2
-10
-5
0
5
10
$\mu_0 H$ (T)
(b)
4
2
0
-2
-4
ρ_{xy} ($\times$ 10^{-2} $\mu\Omega$ cm)
5 X 15 um
I_c
ρ_{xx}
[0$\bar{1}$1]
[$\bar{1}\bar{1}$2]
[$\bar{1}$21]
ρ_{xy}
15 $\times$ 5 μm^2
I_c || [$\bar{1}\bar{1}$2]
2 K
300 K
-10
-5
0
5
10
$\mu_0 H$ (T)

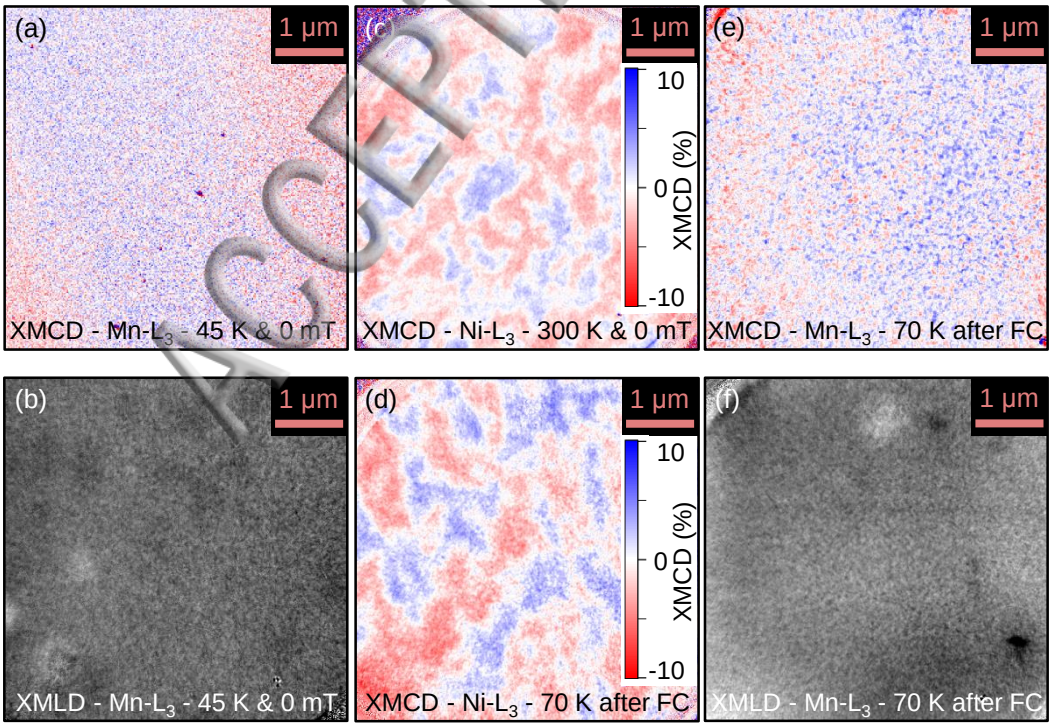
(a)
1 µm
XMCD - Mn-L3 - 45 K & 0 mT
(c)
1 µm
10
0
-10
XMCD (%)
XMCD - Ni-L3 - 300 K & 0 mT
(e)
1 µm
XMCD - Mn-L3 - 70 K after FC
(b)
1 µm
XMLD - Mn-L3 - 45 K & 0 mT
(d)
1 µm
10
0
-10
XMCD (%)
XMCD - Ni-L3 - 70 K after FC
(f)
1 µm
XMLD - Mn-L3 - 70 K after FC